ISSN 1392-1320 MATERIALS SCIENCE (MEDŽIAGOTYRA). Vol. 29, No. 2. 2023

Combinatorial Effects of the Recipes of the Initial Gas-atomized Powder Sizes on Microstructure and Passivation Characteristics of the SLM-ed Ti-6Al-4V Bulk Alloys

Yu ZHANG, Jiazhuo LEI, Zhenhua DAN *, Hui CHANG, Lian ZHOU

College of Materials Science and Engineering, Tech Institute for Advanced Materials, Nanjing Tech University, No. 5 Xinmofan Road, Gulou District, Nanjing 211816, China

https://doi.org/10.5755/j02.ms.31220

Received 28 April 2022; accepted 6 June 2022

Bulk Ti-6Al-4V alloys have been fabricated by selective laser melting (SLM) in three recipes with different combinations of powder sizes. Combinatorial effects of initial gas-atomized powder sizes on microstructure and corrosion properties of SLM-ed Ti-6Al-4V alloys have been investigated by optical microscopy, X-ray diffraction, electrochemical measurements and surface free energy. The SLM-ed Ti-6Al-4V alloys are composed of acicular α' martensite and α phases. Many pinhole defects and twin boundaries exist in the SLM-ed Ti-6Al-4V alloys. According to electrochemical tests and surface free energy calculation, the SLM-ed Ti-6Al-4V alloys with 0 – 53 μm powders have the most positive corrosion potential, the lowest current density and the smallest surface free energy of 20.89 mJ m^2. The passive film of SLM-ed Ti-6Al-4V alloys with 0 – 53 μm powders has superior protection ability due to their large thickness. The carrier concentration of SLM-ed Ti-6Al-4V alloys with 0 – 53 μm powders is the lowest by the Mott-Schottky curves. The SLM-ed samples with contact angles higher than 90° are hydrophobic, but the small contact angle of 46.98° reflects the hydrophilic features of as-rolled Ti-6Al-4V alloys. The combinatorial recipe of SLM-ed Ti-6Al-4V alloys with 0 – 53 μm powders is optimal for improvements on the passivation and corrosion resistance.

Keywords: gas-atomized Ti-6Al-4V powders, combinatorial recipe of powders, selective laser melting, electrochemical properties, passive films.

1. INTRODUCTION

Ti-6Al-4V alloys have been widely used in aerospace, chemical industry and other fields due to their high specific strength, corrosion resistance and good biocompatibility and other excellent characteristics [1 – 6]. Selective Laser Melting (SLM) technology, based on the principle of discrete-layer-superimposition uses the high-energy laser beam to directly melt and accumulate the metal powder raw materials to form dense solid parts with the aid of Computer Aided Design [7 – 10]. Compared with those conventional manufacturing methods for the Ti-6Al-4V alloys, the advantages of SLM can realize the fabrication of near-net-shape metal parts that are difficult to process in a short time. Therefore, Ti-6Al-4V alloys can be fabricated by SLM to meet the requirements of the complex shapes and local repair for the large parts. As well known, the physical characteristics of powders, such as shapes, particle size, fluidity, microstructure, etc., affect their fluidity, powder spreading effect, melting process and molten pool morphology directly. The decrease of D_{50} diameters, surface roughness and fluidity of powders mixtures with the increase of fine particle proportion have been reported before [11]. Some scholars investigated the effects of different particle sizes on the properties of metal parts by additive manufacturing. Guo et al [12] have characterized the properties of as-built parts made of different Ti-6Al-4V powders by hot isostatic pressing (HIP). The volume fraction of equiaxed α phases in the bulks decreases with the increase of powder sizes. Gong et al [13] have also found that the fine particles have the inclusion with small particle sizes and these small particles' inclusions can influence the laser absorption on the powder beds, resulting in imperfections in the SLM-ed parts. The results reported by Iebba [14] show that the powder size affects the internal defects and the formation and distribution of pores are different in the melting process with different particle sizes. These previous researches prove that the morphology and particle size of metallic powders are the key factors for the quality of SLM-ed parts. Therefore, the microstructures of SLM-ed titanium alloys are influenced by the combination of the powder sizes which leads to the distinction in the corrosion properties. The high cooling rates during high-speed laser scanning in SLM processes result in the formation of the fusion defects where the corrosion preferentially occurs and is more serious in acidic solutions [15].

Based on the characterization of the microstructure of SLM-ed Ti-6Al-4V alloys, the microstructure of SLM-ed Ti-6Al-4V alloys is mainly acicular α' phase in prior β grains, which is different from those of traditional Ti-6Al-4V alloys with duplex-phase microstructure [16, 17]. The higher strength and poorer plasticity of SLM-ed Ti-6Al-4V alloys than the as-rolled alloys are ascribed to the metastable α' martensite phases [18]. The presence of the hard acicular α' martensite in the duplex phase matrix plays an important role on the higher microhardness [19]. The difference in the

---

*Corresponding author. Tel.: +86-2583587270.
E-mail: *zhenhuadan@njtech.edu.cn* (Z. Dan)

microstructures might result in the different corrosion behavior between traditional and SLM-ed Ti-6Al-4V alloys. Dai et al [20] have stated that the microstructure of SLM-ed Ti-6Al-4V alloy is mainly composed of acicular α' phases. The XZ-plane of the SLM-ed Ti-6Al-4V alloy is composed of more α'-Ti and less β-Ti phase than the XY-plane, which leads to the inferior corrosion resistance of the XZ-plane. The surface of passive films of alloys occurs pitting due to the action of chloride ions in 3.5 wt.% NaCl solution [20]. The electrochemical impedance spectroscopy of SLM-ed Ti-6Al-4V alloys displays a single capacitive arc and the size of the capacitive arc is proportional to the corrosion resistance in artificial seawater at 20 – 40 ℃ [21], which indicates that the surface passive films might differ from the traditional ones in the chemical compositions or thickness. In comparison to as-cast Ti-6Al-4V alloys, the abundant metastable α′ martensite phases in SLM-ed Ti-6Al-4V alloys cause the different corrosion behaviors reported by Sharma et al [22]. The SLM-ed Ti-6Al-4V alloys have better corrosion resistance due to the hydrophobicity than these wrought and wrought+HT samples [23]. The corrosion resistance of the additively manufactured Ti-6Al-4V alloys becomes better due to the thickening of the passive film and the decrease of carrier concentrations [24 – 26].

The influence of the recipe of the initial Ti-6Al-4V powder sizes on the microstructure and corrosion properties of the Ti-6Al-4V alloys fabricated by selective laser melting processes (SLM) is of importance for the control of the anti-corrosion performances rather than their microstructure and mechanical properties. The microstructure and phase composition of SLM-ed Ti-6Al-4 V alloys with three kinds of powder recipes are to be studied by optical microscopy, X-ray diffractometer and transmission electron microscopy. The electrochemical properties of SLM-ed Ti-6Al-4V alloys with three kinds of powders were analyzed by potentiodynamic scanning, impedance spectroscopy and Mott-Schottky measurements. The combinatorial effects of the initial gas-atomized powder sizes on microstructure and corrosion properties of SLM-ed Ti-6Al-4V alloys are aimed to be revealed from the aspects of the distribution of the defects, the potentiodynamic response, the thickness of the surface passive films and the surface energy.

2. EXPERIMENTAL PROCEDURE

The powders were produced by the electrode induction melting gas atomization process (EIGA). The chemical compositions of the Ti-6Al-4V alloy powders were confirmed to be 87.7 ~ 90.2 wt.% Ti, 5.5 ~ 6.8 wt.% Al, 3.3 ~ 4.5 wt.% V, 0.2 wt.% Fe, 0.2 wt.% C, 0.2 wt.% N, 0.2 wt.% H, 0.2 wt.% O. The powder size distribution was measured by a laser particle size analyzer (Mastersizer 2000). Then the powders were sieved and mixed into three groups (i.e. 15 – 53 μm powder, 0 – 53 μm powder and mixed powder (with a weight ratio of 1:2 of 0 – 25 μm and 15 – 53 μm powders) as listed in Table 1). The Ti-6Al-4V alloys were produced using an EOS 280 system at a scanning rate of 1.2 m/s, a scanning spacing of 140 μm and a laser power of 280 W. Hereafter the SLM-ed samples with different initial powder size combination recipes were abbreviated as No. 1, No. 2 and No. 3. Traditional as-rolled Ti-6Al-4V alloy, as a reference, was being named No. 4. The samples were grounded on SiC sandpaper with grits from 240# to 3000# and were polished. After being mechanically polished with 0.04 micron polishing solution, the samples were etched with Kroll's solution (HF 1 ml, HNO_3 2 ml and H_2O 7 ml). Optical microscopy (OM, Zeiss AxioObsever D1m), scanning electron microscopy (SEM, JEOL JIB-4610) and transmission electron microscopy (TEM, JEOL, HC2100) were employed to analyze the microstructure of SLM-ed Ti-6Al-4V alloys. The width of the acicular α′ martensite was measured by Nano Measurer software over 120 sites. The phase compositions of SLM-ed Ti-6Al-4V alloys and rolled Ti-6Al-4V alloys were analyzed using an X-ray diffractometer (XRD Smart Lab TM 3KW) with Cu Kα1 at a scanning speed of 10°/min in 20° to 90°. The electrochemical measurements including open circuit potential, potentiodynamic polarization curves and electrochemical impedance spectra (EIS) were carried out in 3.5wt.% NaCl and 0.5 M H_2SO_4 solutions in the three-electrode systems. The Ag/AgCl electrode in saturated KCl solution was used as the reference electrode, and all potential here was referred to the Ag/AgCl reference electrode. To figure out the thickness of the passive films, the EIS measurements were performed with an AC frequency ranging from 10^5 Hz to 10^{-2} Hz by applying an amplitude voltage of 10 mV. The polarization curves were conducted at a scan rate of 1 mV/s and in the potential range from -1 V to 0.6 V. The chemical binding states and the chemical composition of the passive films of No. 1 and No. 4 samples were investigated by X-ray photoelectron spectroscopy (XPS, Shimadzu Kratos, AXIS-Ultra DLD) with monochromatized Al K_α excitation ($h\gamma$ = 1486.6 eV). The semiconducting properties of SLM-ed Ti-6Al-4V alloys with different powders were evaluated through Mott-Schottky plots. To investigate the adsorption capacity, the contact angles and surface free energy of different samples were measured by using a surface tensionmeter (Powereach JC2000D3).

Table 1. Recipe of the initial powder sizes for the SLM-ed Ti-6Al-4V alloys

Samples	Particle size, μm	D_{10}, μm	D_{50}, μm	D_{90}, μm
No. 1	0 – 53	14.4	31.7	57.7
No. 2	15 – 53	26.7	40.8	61.8
No. 3	mixed 0 – 25 μm and 15 – 53 μm powders with weight ratio of 1:2	14.3	34.3	61.8
No. 4	Traditional as-rolled Ti-6Al-4V alloy (reference materials)			

3. RESULTS AND DISCUSSION

3.1. Effect of the initial powder sizes on the microstructure and defects of SLM-ed Ti-6Al-4V alloys

The particle size distribution is presented in Fig. 1. According to Fig. 1 a, the particle sizes of three Ti-6Al-4V powders are all normally distributed, and the particle sizes for No. 2 samples are distributed in a narrow range of the powder sizes. There are almost no particles with a particle size of less than 20 μm in 15 – 53 μm powders. The powders for No. 1 occupy a higher portion of fine particles with a powder size less than 10 μm than those for No. 2 samples. As shown in Table 1, the D_{10} of No. 1 ~ No. 3 is confirmed to be 14.4, 26.7 and 14.3 μm, respectively. Their D_{50} values are done to be 31.7, 40.8 and 34.3 μm. Their D_{90} values are very close. Compared with the powers for No. 2 samples, the D_{10} values of No. 1 and No. 3 are reduced by nearly 50 %. The D_{50} values of No. 1 and No. 3 dropped by 16 % and 22 %, respectively. According to Fig. 1 b, the fine powder proportion for No. 1 samples is the highest and 36 %.

The morphology of the three recipes of the EIGA Ti-6Al-4V powders is shown in Fig. 2. The sphericity and surface roughness of small particles are better than those of large particles. According to Fig. 2 a, the powders for No. 1 samples present a highly spherical shape and have a relatively smooth surface. The surface of the powders for No. 2 samples is rough and has a nearly sphericity shape with some oval-shaped satellite powders, as seen in Fig. 2 b. Due to the addition of the fine powders for No. 3 samples, the small powders tend to unit together and attach to the surface of the large powders. The powders for No. 3 samples have many irregular-shaped powders with some satellite spheres attached to the surface in Fig. 2 c. A small amount of fine powders are deformed to adhere to the large powders due to the extrusion of the grinding balls during the mixing process [10, 11]. It can be found that there are the higher proportions of the coarse powders in the powders for No. 2 samples, which might cause the rough microstructure and higher defect density in SLM-ed samples due to the discontinuous distributions in the large gaps between the coarse powders [11, 14].

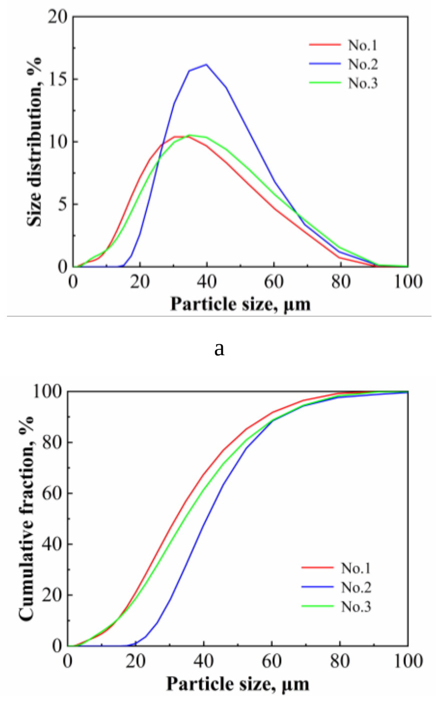

a

b

Fig. 1. a – size distribution; b – a cumulative fraction of different powders (No. 1: 0 – 53 μm, No. 2: 15 – 53 μm, No. 3: mixed Ti-6Al-4V powder in a weight ratio of 1:2 of 0 – 25 μm and 15 – 53 μm powders)

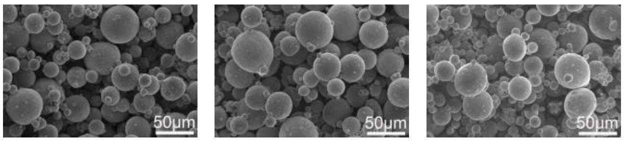

a b c

Fig. 2. Micrographs of different powders: a – 0 – 53 μm powder; b – 15 – 53 μm powder; c – mixed Ti-6Al-4V powder in weight ratio of 1:2 of 0 – 25 μm and 15 53 – μm powders

The phase constitutes and microstructure of SLM-ed samples were identified by XRD, OM, SEM and TEM. The XRD patterns of SLM-ed No. 1 ~ 3 and the bulk samples of No. 4 in Fig. 3 state that No. 1, No. 2 and No. 3 samples are mainly composed of hexagonal closed packed (hcp) α phases and α' martensite.

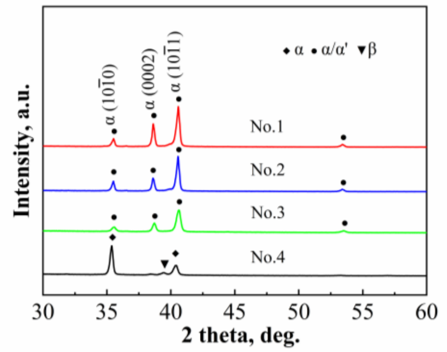

Fig. 3. XRD patterns of different samples (No. 1: 0 – 53 μm, No. 2: 15 – 53 μm, No. 3: mixed Ti-6Al-4V powder in a weight ratio of 1:2 of 0 – 25 μm and 15 – 53 μm powders, No.4: as-rolled Ti-6Al-4V alloy)

According to the (0002) diffraction peak heights, the volume fraction of α phases in No. 1 samples should be higher than others. The phase compositions of the No.4 sample are conformed to be *α* and *β* phases. The high diffraction peak intensity of $(10\bar{1}0)$ α/α′ phases of SLM-ed samples indicates that the high cooling rates and limited elemental diffusions of SLM processes result in the dominant form of the metastable α' martensite. As can be seen in Fig. 4 a – c, the SLM-ed Ti-6Al-4V alloys consist of acicular α' martensite, consistent with XRD results (Fig. 3).

The width of acicular α′ martensite of No. 1, No. 2 and No. 3 samples is 1.02, 0.7, and 0.36 μm. The fractions of α phases No. 1, No. 2 and No. 3 samples have been confirmed to be 15.6 %, 10.4 % and 7.1 %, based on OM and SEM data. Fig. 4 d shows the typical duplex-phase microstructure of traditional rolled Ti-6Al-4V alloys with α phases of the volume fraction of 13.2 %.

Due to the high cooling rates (10^3 ~ 10^8 K/s) in SLM processes in comparison to the critical cooling rate (about 410 K/s), the β phases have no time to undergo the phase transformation into the α phases with hcp structure and are transformed into acicular martensite through martensitic transformation [27 – 29]. The yield stress, ultimate tensile stress and elastic modulus of the SLM-ed Ti-6Al-4V alloys with 1 – 80 μm powders are 1156 MPa, 1228 MPa and 130 GPa, respectively [28]. The strength of traditional Ti-6Al-4V alloys is generally 900 ~ 1050 MPa, and the elongation is greater than 10 % [30].

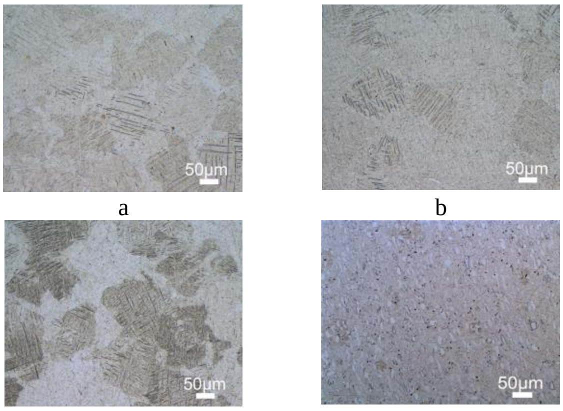

a b c d

Fig. 4. Low-magnified microstructure of different samples in OM mode: a – 0 – 53 μm; b – 15 – 53 μm; c – mixed Ti-6Al-4V powders in weight ratio of 1:2 of 0 – 25 μm and 15 – 53 μm powders; d – as-rolled Ti-6Al-4V alloy

The tensile strength of Ti-6Al-4V alloys formed by SLM is much higher than that of as-rolled Ti-6Al-4V alloys, but the plasticity is poor, caused by the martensite α' phase. The microhardness of different samples is 452.7 $HV_{0.2}$, 423.9 $HV_{0.2}$, 414.0 $HV_{0.2}$ and 340.6 $HV_{0.2}$, respectively, which is consistent with the previous reports [18, 19]. According to Fig. 5, the No. 2 and No. 3 samples are more prone to defects than the No. 1 samples. The structural features of No. 1 SLM-ed samples are shown in Fig. 6 a and b. The SLM-ed samples consist of both lamellar and acicular phases. The twin morphology and electron diffraction are presented in Fig. 6 c and d. A large number of twins can be found in the lamellar. The twins disappear near the boundary of these martensite plates and do not cross the martensite boundary. The generation of these twins is related to the rapid heating and cooling of the laser melting forming in the selected area and the large thermal stress.

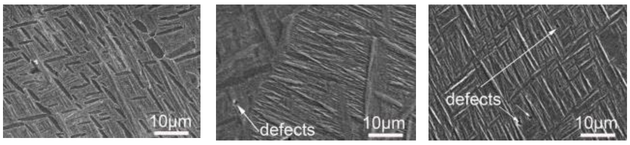

a b c

Fig. 5. High-magnified microstructure of SLM-ed alloys with different powders in SEM mode: a – 0 – 53 μm; b – 15 – 53 μm; c – mixed Ti-6Al-4V powders in weight ratio of 1:2 of 0 – 25 μm and 15 – 53 μm powders

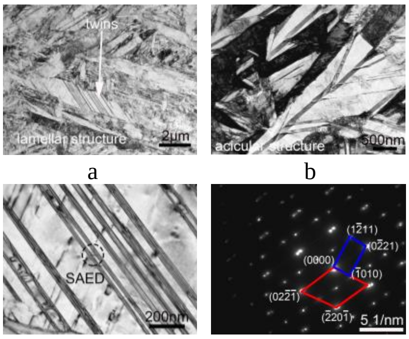

a b c d

Fig. 6. TEM images of No.1 SLM-ed Ti-6Al-4V samples: a – lamellar structure (α'); b – acicular structure; c – twins in lamellar structure; d – SAED patterns of twins

3.2. Electrochemical behavior of SLM-ed Ti-6Al-4V alloys with three recipes of the initial powder sizes

Fig. 7 a shows the polarization curves of SLM-ed Ti-6Al-4V alloys with three recipes of the initial powder sizes in 3.5 wt.% NaCl solution. The fluctuations of current density ranging from -0.2 to 0.1 V reflect the passivation-dissolution-repassivation of the surface passive films of No. 1, No. 2 and No. 3. Although the fluctuations of the currents of No. 1 samples are large, they can repassivate at the lower levels than others. Cl^- ions, as well-known causative agents, are adsorbed into the interior of the oxide film on the metal and the surface of passive films and chemically induce the breakdown of the passive films [31]. The corrosion parameters extracted from the polarization curves are shown in Fig. 7 b.

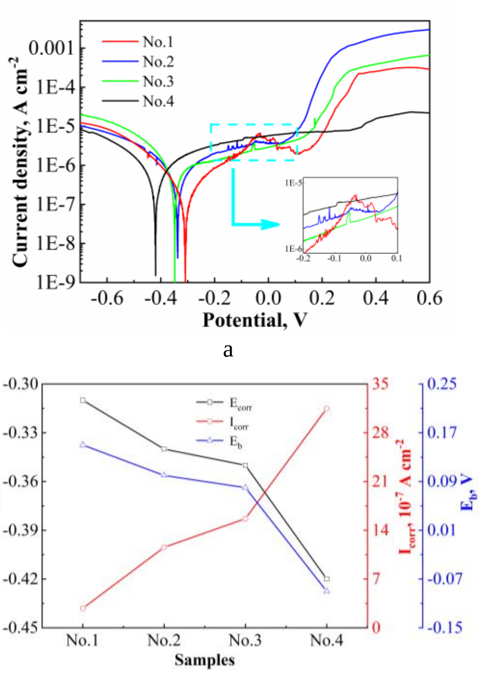

b

Fig. 7. a – polarization curves; b – the values of E_{corr}, I_{corr} and E_b of different samples in 3.5 wt.% NaCl solution (No. 1: 0 – 53 μm, No. 2: 15 – 53 μm, No. 3: mix7ed Ti-6Al-4V powder in a weight ratio of 1:2 of 0 – 25 μm and 15 – 53 μm powders, No. 4: as-rolled Ti-6Al-4V alloy)

The E_{corr} of the No. 1, No. 2 No. 3 and No. 4 samples are confirmed to be -0.31, -0.34, -0.35 and -0.42 V, respectively. The E_{corr} of the No. 1 sample is the most positive, 30 mV higher than No. 2 sample, 40 mV higher than No. 3 and 110 mV higher than No. 4 samples. The corrosion current density of No. 1, No. 2 and No. 3 samples is 2.81×10^{-7}, 11.55×10^{-7} and 15.67×10^{-7} A cm^{-2}, respectively. The corrosion current density of the No. 4 sample is 31.48×10^{-7} A cm^{-2}. No. 1 sample with the smallest corrosion current density and highest corrosion potential among all samples might be attributed to the thickness of the surface passive films.

The Nyquist plots of different samples in 3.5 wt.% NaCl solution are shown in Fig. 8 a. All the SLM-ed Ti-6Al-4V alloys exhibit a larger size of capacitive reactance arc than as-rolled alloys. In general, the diameters of the capacitive reactance arcs have a great relationship with the corrosion resistance. The corrosion resistances become better with the larger capacitive reactance arcs [32], and the No. 1 sample has the most optimal corrosion resistance. The inset in Fig. 8 a displays the equivalent circuit (EC) for fitting the EIS results.

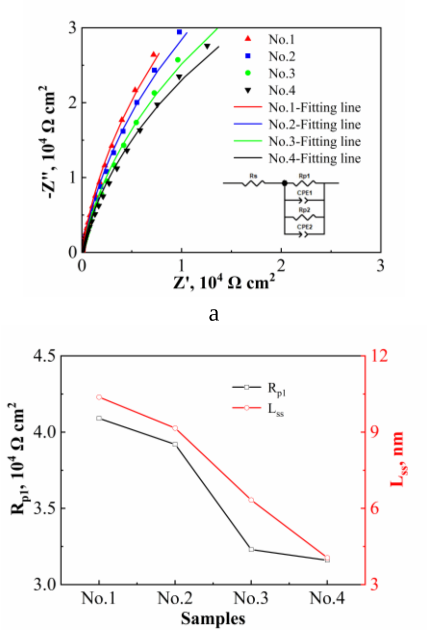

a

b

Fig. 8. a – Nyquist plots; b – R_{p1} values of and L_{ss} of different samples in 3.5wt.% NaCl solution

The equivalent circuit model consists of an electrolyte solution resistance (R_s), constant phase element (CPE_1) for passive oxide film, charge transfer resistance (R_{p1}), constant phase element (CPE_2) for electrochemical double layer and the polarization resistance (R_{p2}). The capacitance is defined by Eq. 1:

$$C = ({R_{p1}}^{1-n} CPE_1)^{1/n}, \qquad (1)$$

where R_{p1} is the charge transfer resistance; n is an exponent of CPE_1. The passive film thickness (L_{ss}) can be estimated based on the parallel plate expression in Eq. 2 [33]:

$$L_{ss} = \frac{\varepsilon \varepsilon_0 A}{C}, \qquad (2)$$

where ε is the dielectric constant of the passive film on Ti-6Al-4V alloys (assumed to be equal to 45 F cm^{-1}), ε_0 is the vacuum dielectric constant (8.854 × 10^{-14} F cm^{-1}) [34], and A is the surface area of the specimen (1 cm^2). The fitted results are shown in Fig. 8 b. The R_{p1} values of No. 1, No. 2, No. 3 and No. 4 samples are 4.09 × 10^5, 3.92 × 10^5, 3.23 × 10^5 and 3.16 × 10^5 Ω cm^2, respectively. The R_{p1} values of SLM-ed Ti-6Al-4V alloys are larger than that of as-rolled Ti-6Al-4V alloys. The L_{ss} values of No. 1, No. 2, No. 3 and No. 4 samples are calculated to be 10.4, 9.2, 6.33 and 4.06 nm, respectively. Particularly, No. 1 sample has the highest R_{p1} of 4.09 × 10^5 Ω cm^2 and the largest L_{ss} of 10.4 nm, indicating that No. 1 sample has better corrosion resistance than other specimens. It is worth noting that the passive films on as-rolled Ti-6Al-4V alloys are much thinner than those of SLM-ed ones. Moreover, the breakdown potential reflects the protective ability of the passive films. The E_b of No. 1, No. 2, No. 3 and No. 4 samples is 0.15, 0.1, 0.08 and -0.09 V, respectively, indicating that the passive films of No. 1 sample have a better protective ability than others.

Fig. 9 a shows the polarization curves of all samples in 0.5 M H_2SO_4 solution. The polarization curves of all samples have a passivation platform and the passivation state becomes similar eventually. It can be seen that the current density of No. 1 and No. 3 samples has potential fluctuation in the range of -0.05 – 0.1 V and 0.05 – 0.3 V, respectively, indicating that the surface passive films occur dissolution and passivation. The electrochemical parameters in Fig. 9 b show that the E_{corr} of the No. 1, No. 2, No. 3 and No. 4 samples is -0.4, -0.47, -0.51 and -0.56 V and the corrosion current density of the No. 1, No. 2, No. 3 and No. 4 samples is 1.13 × 10^{-6}, 5.08 × 10^{-6}, 10.18 × 10^{-6} and 15.64 × 10^{-6} A cm^{-2}, respectively. The No.1 sample has the most positive E_{corr} and the smallest I_{corr}, which indicates No. 1 sample has the best corrosion resistance in 0.5 M H_2SO_4 solution.

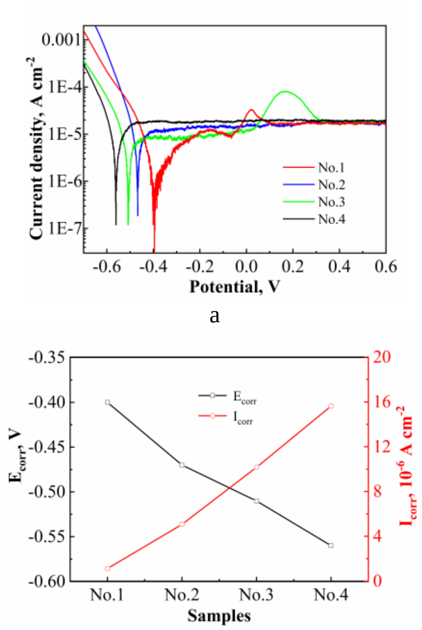

a

b

Fig. 9. a – polarization curves; b – the values of E_{corr} and I_{corr} of different samples in 0.5 M H_2SO_4 solution (No. 1: 0 – 53 μm, No. 2: 0 – 53 μm, No. 3: mixed Ti-6Al-4V powder in a weight ratio of 1:2 of 0 – 25 μm and 15 – 53 μm powders, No. 4: as-rolled Ti-6Al-4V alloy)

The identical difference in the capacitive arcs of different samples in the 0.5 M H_2SO_4 solution can be seen in Fig. 10 a. The capacitive reactance arc reflects the charge transfer on the metal/solution interface [35]. The larger the capacitive reactance arc, the greater the corrosion resistance [36, 37]. Hence, the native oxide layer of No. 1 sample has the best corrosion. The values of R_{p1} and L_{ss} of different samples in 0.5 M H_2SO_4 solution are calculated, and shown in Fig. 10 b.

The R_{p1} values of No. 1, No. 2, No. 3 and No. 4 samples are 54, 50, 49 and 46 Ω cm^2, respectively. The R_{p1} values of SLM-ed Ti-6Al-4V alloys are larger than that of as-rolled Ti-6Al-4V alloys. The L_{ss} values of No. 1, No. 2, No. 3 and No. 4 samples are 12.6, 10.5, 9.7 and 4.8 nm, respectively. Particularly, the No. 1 sample has the highest R_{p1} (54.09 Ω cm^2) and the largest L_{ss} (12.6 nm), indicating that the No. 1 sample has better corrosion resistance than others in 0.5 M H_2SO_4 solution.

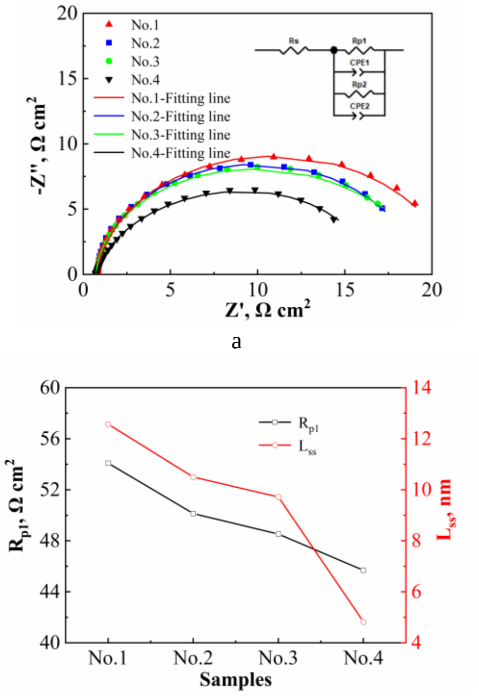

a

b

Fig. 10. a – Nyquist plots; b – the values of $R_{\rm p1}$ and $L_{\rm ss}$ of all samples in 0.5 M H_2SO_4 solution

The change regularity of corrosion resistance of different samples in 0.5 M H_2SO_4 solution is consistent with that in 3.5 wt.% NaCl solution.

XPS spectra, the valent states and the ratios of the SLM-ed alloys (No. 1) and as-rolled alloys (No. 4) are shown in Fig. 11 and Table 2.

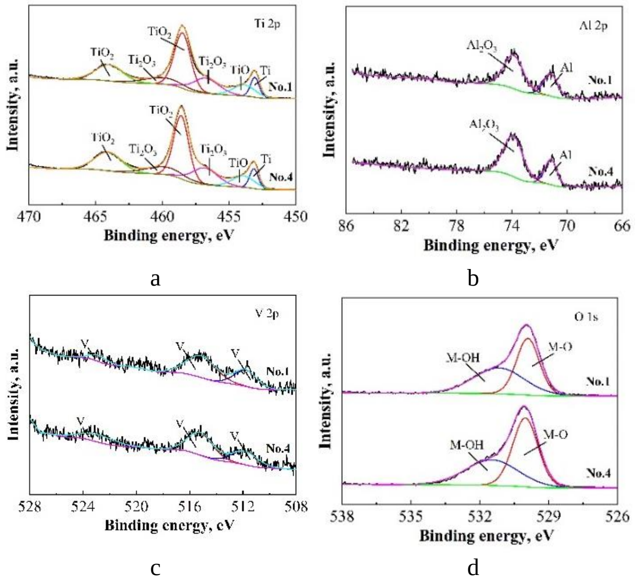

a

b

c

d

Fig. 11. High-resolution spectra of No. 1 and No. 4 samples: a – Ti 2p; b – Al 2p; c – V 2p; d – O 1s. Solid and dashed lines represent measured and fitted spectra

The doublet peaks at 453.13 eV for Ti 2p1/3 and 458.53 eV Ti 2p2/3, and the satellite peaks from the No. 1 sample indicate that Ti element exists in the valent form of Ti^{4+}, $Ti^{2+}$and Ti^0 in Fig. 11 a. The peak shift 0.01 eV of binding energy for the Ti 2p2/3 peak is detected. The Al 2p spectra for No. 1 and No. 4 samples in Fig. 11 b suggests metallic Al and Al_2O_3.

Table 2. The valent state and ratios of the Ti, Al and V elements in the passive films of No. 1 and No. 4 samples

Samples	Elements	Valent state	Ratios, %
No. 1	Ti	Ti^0	2.0
		Ti^{2+}	2.9
		Ti^{3+}	14.7
		Ti^{4+}	7.1
	Al	Al^0	1.6
		Al^{3+}	3.4
	V	V^0	0.9
No. 4	Ti	Ti^0	1.7
		Ti^{2+}	2.6
		Ti^{3+}	14.8
		Ti^{4+}	7.4
	Al	Al^0	1.7
		Al^{3+}	4.4
	V	V^0	0.8

The V elements exist in the form of metallic V instead of V_2O_5 (Fig. 11 c). The proportion of metallic V of No. 1 and No. 4 samples is much lower than the designed one due to the higher Gibbs free energy for the formation, which is consistent with the previous reports [38 – 40]. The subpeaks in O 1s spectra for No. 1 and No. 4 samples belong to M-OH and M-O bonds (Fig. 11 d). The binding energy of M-OH bonds for the No. 1 sample is 530.08 eV and 0.1 eV higher than that for the No. 4 sample. The passive films of No. 1 and No. 4 samples are mainly composed of TiO, TiO_2, Ti_2O_3 and minor Al_2O_3.

The Mott-Schottky plots and donor density of different samples are illustrated in Fig. 12. As shown in Fig. 12 a, the slopes of the Mott-Schottky curves of different samples are all positive, indicating that the passive films of different samples all exhibit typical *n*-type semiconductor characteristics [41]. The semiconducting properties of the passive films can be evaluated by the Mott-Schottky relationship as follows [42]:

$$\frac{1}{C^2}=\frac{2}{\varepsilon\varepsilon_0 eN_d}(E-E_{fb}-\frac{kT}{e}), \qquad (3)$$

where ε_0 is the vacuum dielectric constant (8.85×10^{-14} F cm^{-1}); ε 45 is the relative dielectric constant of passive films [43]; e is the electro charge; N_d is the donor density at the film/metal interface; E_{fb} is the flat band potential, k is the Boltzmann constant and T is the absolute temperature. The $N_{\rm d}$ can be calculated by Eq. 3, as shown in Fig. 12 b. The $N_{\rm d}$ of No. 1, No. 2, No. 3 and No. 4 samples is 1.1×10^{22}, 1.3×10^{22}, 1.5×10^{22} and 3.0×10^{22} cm^{-3}, respectively. Based on point defect theory of the passive films [44], when the carrier concentration in the passive films of alloys becomes lower and the oxygen vacancy content becomes higher with the increase of linear fitting slope, the alloys have the better corrosion resistance [45]. As shown in Fig. 12 b, the donor density of the passive film of the No. 1 sample is lower than others, which leads to the best corrosion resistance of the No. 1 sample.

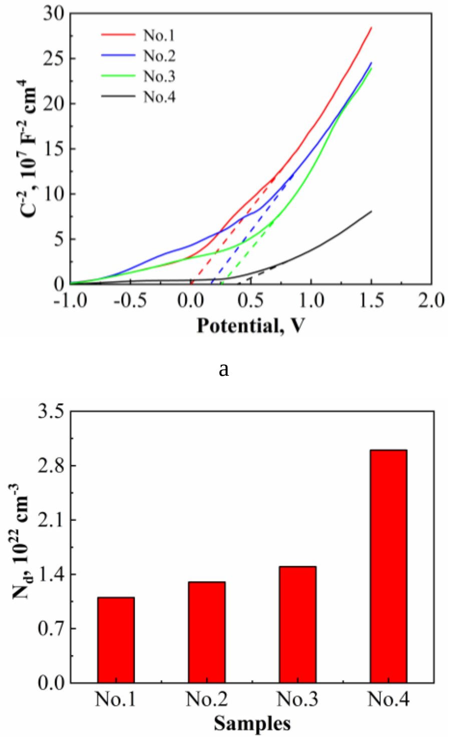

a

b

Fig. 12. a – Mott-Schottky plots of passive films on the surface; b – N$_d$ of different samples in 3.5 wt.% NaCl solution (No. 1: 0 – 53 μm, No. 2: 15 – 53 μm, No. 3: mixed Ti-6Al-4V powder in weight ratio of 1:2 of 0 – 25 μm and 15 – 53 μm powders, No.4: as-rolled Ti-6Al-4V alloy)

The contact angles of distilled water on the different samples are carried out. The contact angles of SLM-ed samples with different Ti-6Al-4V powders are all higher than 90° indicating that the surfaces of SLM-ed samples are hydrophobic features and the surfaces of commercial Ti-6Al-4V alloys are hydrophilic features in Fig. 13. Surface free energies of different samples are calculated by Eq. 4 and Eq. 5 [46]:

$$\gamma_L(1+\cos\theta)=2\sqrt{\gamma_S^D\gamma_L^D}+2\sqrt{\gamma_S^P\gamma_L^P}; \tag{4}$$

$$\gamma_s=\gamma_s^D+\gamma_S^P, \tag{5}$$

where γ_L is the interfacial free energy of liquid-gas per unit area, γ_S^D and γ_L^D are the discrete parts of the free energy of the solid and liquid surface, γ_S^P and γ_L^P are the polar parts of the free energy of the solid and liquid surfaces, γ_s is the surface free energy of the solid, θ is a contact angle on a solid surface. The surface energies were calculated to be 20.1 mJ m^{-2} for the No. 1 sample, 21.4 mJ m^{-2} for No. 2 sample, 24.2 mJ m^{-2} for the No. 3 sample and 55.2 mJ m^{-2} for the No. 4 sample, respectively. The as-rolled Ti-6Al-4V alloy has the highest surface free energy of 55.19 mJ m^{-2} and the surface free energy of the SLM-ed sample with 0 – 53 μm powder is the lowest. The fine powder content of 0 – 53 μm powder is the highest and the surface roughness of SLM-ed alloys with 0 – 53 μm powder is the lowest. The surface roughness has an effect on the wettability of solid surfaces. The surfaces are more easily wetted by the corrosive media and the adsorption performances become better when the contact angles are smaller or the surface energy is higher [47]. Therefore, the as-rolled Ti-6Al-4V alloys with higher surface energy are more likely to react with external media than SLM-ed Ti-6Al-4V alloys. Combining with capacitive semi-loops of different samples (Fig. 8 and Fig. 10), it can be found that the corrosion resistance of SLM-ed Ti-6Al-4V samples is better than as-rolled alloys and the No. 1 sample has the best corrosion resistance, which is considered to be the thicker passive films and lower defect density.

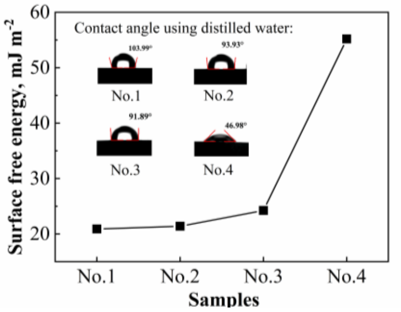

Fig. 13. Surface free energy of different samples (No. 1: 0 – 53 μm, No.2: 15 – 53 μm, No.3: mixed Ti-6Al-4V powder in a weight ratio of 1:2 of 0 – 25 μm and 15 – 53 μm powders, No.4: as-rolled Ti-6Al-4V alloy)

3.3. Discussion

In the different recipes of the initial powder sizes for No. 1, No. 2 and No. 3, the different morphology with different defect distribution, the volume fractions of α/α' phases have been achieved. Based on the size distribution of the initial powders (Fig. 1 and Fig. 2), the phase constitutes of the different samples by XRD (Fig. 3) and features of the SLM-ed microstructure and defects by SEM and TEM analysis (Fig. 5 and Fig. 6), the powders for No. 1 (0 – 53 μm powders) have more portions of the intermediate fine powders which help to fill into the gaps between the large-sized powders coarse powder particles and form the microstructures with less defects. The higher α phases in No. 1 are considered to be due to the accumulation of the more uniform heat distribution during SLM [14, 48]. Moreover, the thickness of the passive films differs much for the different recipes of the initial powder sizes for No. 1, No. 2 and No. 3, as shown in Fig. 8 b and Fig. 10 b. The fine powders with a much larger surface area mean that the higher oxygen content in the SLM-ed samples, which is good for the formation of the passive films due to the higher concentration gradient [11, 14, 49]. The decrease of the binding energy indicates that the oxygen vacancy densities of the No. 4 sample increase and were higher than the No. 1 sample [50]. At the same time, the point defect model proposed by Macdonald [45] points out that the growth of the surface passive films in the solution is due to the generation of oxygen ion vacancies at the interface between the alloys and the passive films. The oxygen atoms can enter the solution or the solution/passive film interface, resulting in the growth of surface passive films. It is worth noting that the thickness of the passive films of SLM-ed samples is much higher than that of as-rolled Ti-6Al-4V alloys. The thicker passive films (10.4 nm in NaCl solution and 12.6 nm in H$_2$SO$_4$ solution) in Fig. 8 b and Fig. 10 b, the less defects in Fig. 5 and lower donor density in Fig. 12 for No. 1 samples than others are responsible for the better performances in Fig. 7 and Fig. 9 and lower surface energy in Fig. 13. On the other hand, the content of the α/α' phases affects the corrosion performances [2, 5, 51, 52]. The corrosion resistance of SLM-ed Ti-6Al-4V alloys become better as the volume fraction of α phases increase. The acicular α' martensite phases with higher electrochemical activities are highly sensitive to pitting and hydrogen embrittlement in the presence of acidic media [17, 18, 53]. The combinatorial recipe of No. 1 is optimal for reducing the appearance of the pinhole defects and twin boundaries. According to the above stated results, the SLM-printed Ti-6Al-4V alloys for the recipe of 0 – 53 μm powders combination has the best passivation and corrosion resistance.

4. CONCLUSIONS

Ti-6Al-4V alloys were produced by SLM technology using different combinatorial recipes of the initial powder sizes of Ti-6Al-4V powders. Based on the analysis of the microstructure and corrosion properties characterized by XRD, optical microscopy, SEM and TEM methods, the combinatorial effects of the recipes of the initial powder sizes on microstructure and electrochemical properties were analyzed. SLM-ed alloys are composed of hcp α and martensite α' phases. No. 1 sample has the least defects among all SLM-ed and as-rolled Ti-6Al-4V alloys. The volume fractions of α phases in No.1 samples are higher than in others. The different behavior of the breakdown and repassivation of all SLM-ed alloys is resulted from the defects, twin boundary. Among SLM-ed alloys, the combinatorial recipe of No. 1 is optimal for reducing the appearance of the pinhole defects and twin boundaries due to the higher portion of the fine powders. The surfaces of SLM-ed Ti-6Al-4V alloys are all hydrophobic features, but that of as-rolled Ti-6Al-4V alloys are hydrophilic. The passivation and corrosion resistance of the No. 1 sample is the best due to its passive films with a larger thickness, less donor density and higher volume fractions of α phases.

Acknowledgments

This work is financially supported by Open Project of Taihu Laboratory of Deep-Sea Technology Science, the National Natural Science Foundation of China (Grant No. 51671106 and 51931008), Key Research and Development Plan of Jiangsu Province (BE2019119). This work is partially supported by Priority Academic Program Development of Jiangsu Higher Education Institution (PAPD).

REFERENCES

1. **Feng, X.T., Lei, J.B., Gu, H., Zhou, S.F.** Effect of Scanning Speeds on Electrochemical Corrosion Resistance of Laser Cladding TC4 Alloy *Chinese Physics B* 28 2019: pp. 383 – 390. https://doi.org/10.1088/1674-1056/28/2/026802
2. **Gao, J.B., Zhao, X.L., Yue, J.K., Qi, M.C, Zhang, D.L.** Microstructure and Mechanical Properties of Ti-6Al-4V Alloy Samples Fabricated by Selective Laser Melting *Key Engineering Materials* 770 2018: pp. 179 – 186. https://doi.org/10.4028/www.scientific.net/KEM.770.179
3. **Atar, E., Kayali, E.S., Cimenoglu, H.** Characteristics and Wear Performance of Borided Ti6Al4V Alloy *Surface & Coatings Technology* 202 (19) 2008: pp. 4583 – 4590. https://doi.org/10.1016/j.surfcoat.2008.03.011
4. **Revathi, A., Vijayalakshmi, U., Geetha, M.** Comparative Study of Electrochemical Behaviour of CP-titanium and Ti–6Al–4V with Other Titanium Based Alloys for Biomedical Applications *Materials Technology* 29 (B1) 2014: pp. B49 – B53. https://doi.org/10.1179/1753555713Y.0000000109
5. **Aaya-Vazquez, M.R., Sánchez-Amaya, J.M., Boukha, Z., Botana, F.J.** Microstructure, Microhardness and Corrosion Resistance of Remelted TiG2 and Ti–6Al–4V by a High Power Diode Laser *Corrosion Science* 56 2012: pp. 36 – 48. https://doi.org/10.1016/j.corsci.2011.11.006
6. **Yadroitse, Y., Krakhmaley, P., Yadroitsava, I.** Selective Laser Melting of Ti6Al4V Alloy for Biomedical Applications: Temperature Monitoring and Microstructural Evolution *Journal of Alloys and Compounds* 583 2014: pp. 404 – 409. https://doi.org/10.1016/j.jallcom.2013.08.183
7. **Simonelli, M., Tse, Y.Y., Tuck, C.** Effect of the build orientation on the mechanical properties and fracture modes of SLM Ti–6Al–4V *Materials Science and Engineering: A* 616 2014: pp. 1 – 11. https://doi.org/10.1016/j.msea.2014.07.086
8. **Ellyson, B., Brochu, M., Brochu, M.** Characterization of bending vibration fatigue of SLM fabricated Ti-6Al-4V *International Journal of Fatigue* 99 2017: pp. 25 – 34. https://doi.org/10.1016/j.ijfatigue.2017.02.005
9. **Attar, H., Calin, M., Zhang, L.C., Scudino, S., Eckert, J.** Manufacture by Selective Laser Melting and Mechanical Behavior of Commercially Pure Titanium *Materials Science & Engineering A* 593 (1) 2014: pp. 170 – 177. https://doi.org/10.1016/j.msea.2013.11.038
10. **Zhou, B., Zhou, J., Li, H.X., Lin, F.** A Study of the Microstructures and Mechanical Properties of Ti6Al4V Fabricated by SLM under Vacuum *Materials Science & Engineering A* 724 2018: pp. 1 – 10. https://doi.org/10.1016/j.msea.2018.03.021
11. **Zhang, S.C., Sun, Z.G., Liang, Z.L., Zhang, W.S., Chen, X.L., Chang, H.** Effect of Powder Properties and Heat Treatment on Microstructure Evolution of Selective Laser Melted Titanium Alloy *Rare Metal Materials and Engineering* 48 (10) 2019: pp. 3234 – 3240. https://doi.org/CNKI:SUN:COSE.0.2019-10-025
12. **Guo, R.P., Yu, B.B., Shi, X.H., Xu, L., Yang, R.** Effect of Powder Size on Fatigue Properties of Ti–6Al–4V Powder Compact using Hot Isostatic Pressing *JOM* 71 2019: pp. 3614 – 3620. https://doi.org/10.1007/s11837-019-03612-7
13. **Gong, H.J., Dilip, J.J.S., Yang, L., Teng, C., Stucker, B.** Influence of Small Particles Inclusion on Selective Laser Melting of Ti–6Al–4V Powder *IOP Conference Series: Materials Science and Engineering* 272 2017: pp. 012024. https://doi.org/10.1088/1757-899X/272/1/012024
14. **Iebba, M., Astarita, A., Mistretta, D., Colonna, I., Liberini, M., Scherillo, F., Pirozzi, C., Borrelli, R., -Franchitti, S., Squillace, A.** Influence of Powder Characteristics on Formation of Porosity in Additive Manufacturing of Ti-6Al-4V Components *Journal of Materials Engineering & Performance* 26 (3) 2017: pp. 4138 – 4147. https://doi.org/10.1007/s11665-017-2796-2

15. **Li, Y.M., Liu, C., Liang, Y.H., Chen, X.T., Yang, Z.B., Chen, Y.J.** The Long-term Corrosion Behaviors of SLM 316L Stainless Steel Immersed in Artificial Saliva *Materials Science (Medžiagotyra)* 28 (2) 2022: pp. 196 – 201. http://dx.doi.org/10.5755/j02.ms.28636
16. **Yan, X.C., Yin, S., Chen, C.Y., Huang, C.J., Bolot, R., Lupoi, R., Kuang, M., Ma, W.Y., Coddet, C., Liao, H.L., Liu, M.** Effect of Heat Treatment on the Phase Transformation and Mechanical Properties of Ti6Al4V Fabricated by Selective Laser Melting *Journal of Alloys and Compounds* 764 2018: pp. 1056 – 1071. https://doi.org/10.1016/j.jallcom.2018.06.076
17. **Xu, Y.L., Zhang, D.Y., Guo, Y.W., Hu, S.T., Wu, X.P., Jiang, Y.J.** Microstructural Tailoring of As-Selective Laser Melted Ti6Al4V Alloy for High Mechanical Properties *Journal of Alloys and Compounds* 816 2020: pp. 152536. https://doi.org/10.1016/j.jallcom.2019.152536
18. **Köse, C., Karaca, E.** Robotic Nd:YAG Fiber Laser Welding of Ti-6Al-4V Alloy *Metals* 7 2017: pp. 221 – 231. https://doi.org/10.3390/met7060221
19. **Köse, C., Karaca, E.** Effect of Pre and Post Weld Heat Treatments on the Microstructure and Mechanical Properties of Robotic Fiber Laser Welded Ti-6Al-4V Alloy *Archives of Metallurgy & Materials* 63 2018: pp. 1225 – 1233. https://doi.org/10.24425/123795
20. **Dai, N.W., Zhang, L.C., Zhang, J.X., Zhang, X., Ni, Q.Z., Chen, Y., Wu, M.L., Yang, C.** Distinction in Corrosion Resistance of Selective Laser Melted Ti-6Al-4V alloy on Different Planes *Corrosion Science* 111 2016: pp. 703 – 710. https://doi.org/10.1016/j.corsci.2016.06.009
21. **Zhang, Y.F., Li, J.Z., Zhang, W.H.** Electrochemical Behavior and Corrosion Properties of Ti–6Al–4V Alloy Made by Selective Laser Melting for Immersion in Artificial Seawater at Different Temperature *Characterization of Minerals, Metals and Materials TMS 2018* 2018: pp. 61 – 72. https://doi.org/10.1007/978-3-319-72484-3_7
22. **Sharma, A., Oh, M.C., Kim, J.T., Srivastava, A.K., Ahn, B.** Investigation of Electrochemical Corrosion Behavior of Additive Manufactured Ti-6Al-4V Alloy for Medical Implants in Different Electrolytes *Journal of Alloys and Compounds* 830 2016: pp. 154620. https://doi.org/10.1016/j.jallcom.2020.154620
23. **Ju, J., Li, J.J., Jiang, M., Li, M.Y., Yang, L.X., Wang, K.M., Yang, C., Kang, M.D., Wang, J.** Microstructure and Electrochemical Corrosion Behavior of Selective Laser Melted Ti6Al4V Alloy in Simulated Artificial Saliva *Transactions of Nonferrous Metals Society of China* 31 (1) 2021: pp. 167 – 177. https://doi.org/10.1016/S1003-6326(20)65485-1
24. **Chiu, T.M., Mahmoudi, M., Dai, W., Elwany, A., Liang, H., Castaneda, H.** Corrosion Assessment of Ti–6Al–4V Fabricated using Laser Powder-bed Fusion Additive Manufacturing *Electrochimica Acta* 279 2018: pp. 143 – 151. https://doi.org/10.1016/j.electacta.2018.04.189
25. **Zhou, X., Xu, D., Geng, S., Fan, Y., Wang, F.** Microstructural Evolution and Corrosion Behavior of Ti–6Al–4V Alloy Fabricated by Laser Metal Deposition for Dental Applications *Journal of Materials Research and Technology* 14 2021: pp. 1459 – 1472. https://doi.org/10.1016/j.jmrt.2021.07.006
26. **Seo, D.I., Lee, J.B.** Effects of Competitive Anion Adsorption (Br− or Cl−) and Semiconducting Properties of the Passive Films on the Corrosion Behavior of the Additively Manufactured Ti-6Al-4V Alloys *Corrosion Science* 173 2020: pp. 108789. https://doi.org/10.1016/j.corsci.2020.108789
27. **He, B.B., Wu, W.H., Zhang, L., Lu, L., Yang, Q.Y.** Microstructural Characteristic and Mechanical Property of Ti6Al4V Alloy Fabricated by Selective Laser Melting *Vacuum* 150 2018: pp. 79 – 83. https://doi.org/10.1016/j.vacuum.2018.01.026
28. **Liang, Z.L., Sun, Z.G., Zhang, W.S., Wu, S.K., Chang, H.** The Effect of Heat Treatment on Microstructure Evolution and Tensile Properties of Selective Laser Melted Ti6Al4V Alloy *Journal of Alloys and Compounds* 782 2019: pp. 1041 – 1048. https://doi.org/10.1016/j.jallcom.2018.12.051
29. **Thijs, L., Verhaeghe, F., Craeghs, T., Humbeeck, J.V., Kruth, J.P.** A Study of the Microstructural Evolution during Selective Laser Melting of Ti-6Al-4V *Acta Materialia* 58 (9) 2010: pp. 3303 – 3312. https://doi.org/10.1016/j.actamat.2010.02.004
30. **Xu, Y., Yang, X.J., Le, W., Du, D.N.** Microstructure and Mechanical Properties of TC4 Titanium Alloy by Multi-pass Rolling *Special Casting & Nonferrous Alloys* 37 2017: pp. 697 – 700. https://doi.org/10.15980/j.tzzz.2017.07.001
31. **Yang, J.J., Yang, H.H., Yu, H.C., Wang, Z.M., Zeng, X.Y.** Corrosion Behavior of Additive Manufactured Ti–6Al–4V Alloy in NaCl Solution *Metallurgical & Materials Transactions A Physical Metallurgy & Materials Science* 48 2017: pp. 3583 – 3593. https://doi.org/10.1007/s11661-017-4087-9
32. **Qin, T., Lin, X., Yu, J., Wang, M., Guo, P.F., Li, J.Q., Zhang, Y.F., Liu, J.R., Zhang, S.L., Huang, W.D.** Performance of Different Microstructure on Electrochemical Behaviors of Laser Solid Formed Ti-6Al-4V Alloy in NaCl Solution *Corrosion Science* 185 (11) 2021: pp. 109392. https://doi.org/10.1016/j.corsci.2021.109392
33. **Zakerin, N., Morshed-Behbahani, K.** In Vitro Electrochemical Behavior of Aged Ti-6Al-4V Alloy: a Trial of the Point Defect Model *Materials Today Communications* 27 2021: pp. 102327. https://doi.org/10.1016/j.mtcomm.2021.102327
34. **Milošev, I., Kosec, T., Strehblow, H.** XPS and EIS Study of the Passive Film Formed on Orthopaedic Ti–6Al–7Nb Alloy in Hank's physiological Solution *Electrochimica Acta* 53 (9) 2008: pp. 3547 – 3558. https://doi.org/10.1016/j.electacta.2007.12.041
35. **Guo, K.K., Liu, C.S., Chen, S.Y., Dong, H.H., Wang, S.Y.** High Pressure EIGA Preparation and 3D Printing Capability of Ti-6Al-4V Powder *Transactions of Nonferrous Metals Society of China* 30 (1) 2020: pp. 147 – 159. https://doi.org/10.1016/S1003-6326(19)65187-3
36. **Wang, L., Cheng, X.Q., Gao, S.J., Li, X.G., Zou, S.W.** The Influence Mechanism of Fe^{3+} on Corrosion Behavior of Ti6Al4V in Sulfuric Acid Solutions *Materials and Corrosion* 66 2015: pp. 251 – 256. https://doi.org/10.1002/maco.201307380
37. **Mogoda, A.S., Ahmad, Y.H., Badawy, W.A.** Corrosion Behaviour of Ti-6Al-4V Alloy in Concentrated Hydrochloric and Sulphuric Acids *Journal of Applied Electrochemistry* 34 (9) 2004: pp. 873 – 878. https://doi.org/10.1023/B:JACH.0000040447.26482.bd
38. **Ask, M., Lausmaa, J., Kasemo, B.** Preparation and Surface Spectroscopic Characterization of Oxide Films on Ti6Al4V *Applied Surface Science* 35 (3) 1989: pp. 283 – 301.

https://doi.org/10.1016/0169-4332(89)90013-5

39. **Wu, G.L., Wang, Y., Sun, M., Zhang, Q.L., Yao, J.H.** Influence of Microstructure of TC4 Substrate on the MAO Coating *Surface Engineering* 36 (8) 2020: pp. 827 – 836. https://doi.org/10.1080/02670844.2019.1693732
40. **Vaithilingam, J., Kilsby, S., Goodridge, R.D., Christie, S.D.R., Edmondson, S., Hague, R.J.M.** Functionalisation of Ti6Al4V Components Fabricated Using Selective Laser Melting with a Bioactive Compound *Materials Science and Engineering: C* 46 2015: pp. 52 – 61. https://doi.org/10.1016/j.msec.2014.10.015
41. **Zhang, C.H., Song, W., Wang, Y.M., Xiao, G.Z.** Effect of Surface Strengthening on Corrosion Property of Ti–6Al–4V in 3.5% NaCl *Applied Mechanics & Materials* 853 2016: pp. 473 – 477. https://doi.org/10.4028/www.scientific.net/AMM.853.473
42. **Gai, X., Bai, Y., Li, S.J., Hou, W.T., Hao, Y.L., Zhang, X., Yang, R., Misra, R.D.K.** In-situ Monitoring of the Electrochemical Behavior of Cellular Structured Biomedical Ti–6Al–4V Alloy Fabricated by Electron Beam Melting in Simulated Physiological Fluid *Acta Biomaterialia* 106 2020: pp. 387 – 395. https://doi.org/10.1016/j.actbio.2020.02.008
43. **Roh, B., Macdonald, D.D.** Passivity of Titanium: Part II, the Defect Structure of the Anodic Oxide Film *Journal of Solid State Electrochemistry* 23 (1 – 3) 2019: pp. 1 – 13. https://doi.org/10.1007/s10008-019-04254-0
44. **Jiang, Z.L., Dai, X., Norby, T., Middleton, H.** Investigation of Pitting Resistance of Titanium Based on a Modified Point Defect Model *Corrosion Science* 53 2011: pp. 815 – 821. https://doi.org/10.1016/j.corsci.2010.11.015
45. **Macdonald, D.D.** The history of the point defect model for the passive state: A Brief Review of Film Growth Aspects *Electrochimica Acta* 56 (4) 2011: pp. 1761 – 1772. https://doi.org/10.1016/j.electacta.2010.11.005
46. **Miyajima, H., Awadzi, G., Ozer, F., Mante, F.K.** Effect of Surface Physico-chemico-biological Modifications of Ttanium on Critical and Theoretical Surface Free Energy *Applied Surface Science* 470 2018: pp. 386 – 394. https://doi.org/10.1016/j.apsusc.2018.11.133
47. **Zeng, D.M., Dan, Z.H., Qin, F.X., Chang, H.** Adsorption-enhanced Reductive Degradation of Methyl Orange by $Fe_{73.3}Co_{10}Si_4B_8P_4Cu_{0.7}$ Amorphous Alloys *Materials Chemistry and Physics* 242 2020: pp. 122307. https://doi.org/10.1016/j.matchemphys.2019.122307
48. **Zhu, S., Yang, H., Guo, L.G., Fan, X.G.** Effect of Cooling Rate on Microstructure Evolution during α/β Heat Treatment of TA15 Titanium Alloy *Materials Characterization* 70 2012: pp. 101 – 110. https://doi.org/10.1016/j.matchar.2012.05.009
49. **Schultze, J.W., Stimming, U., Weise, J.** Capacity and Photocurrent Measurements at Passive Titanium Electrodes *Berichte der Bunsengesellschaft für physikalische Chemie* 86 1982: pp. 276 – 282. https://doi.org/10.1002/bbpc.19820860404
50. **Qin, T., Lin, X., Yu, J., Wang, M., Guo, P.F., Li, J.Q., Zhang, Y.F., Liu, J.R., Zhang, S.L., Huang, W.D.** Performance of different microstructure on electrochemical behaviors of laser solid formed Ti-6Al-4V alloy in NaCl solution *Corrosion Science* 185 2021: pp. 109392. https://doi.org/10.1016/j.corsci.2021.109392
51. **Atapour, M., Pilchak, A.L., Frankel, G.S., Williams, J.C., Fathi, M.H., Shamanian, M.** Corrosion Behavior of Ti-6Al-4V with Different Thermomechanical Treatments and Microstructures *Corrosion* 66 (6) 2010: pp. 065004. https://doi.org/10.5006/1.3452400
52. **Atapour, M., Pilchak, A.L., Frankel, G.S., Williams, J.C.** Corrosion Behavior of Friction Stir-processed and Gas Tungsten Arc-welded Ti–6Al–4V *Metallurgical and Materials Transactions A* 41 2010: pp. 2318 – 2327. https://doi.org/10.1007/s11661-010-0304-5
53. **Zhou, L.J., Deng, H., Chen, L.Q., Qiu, W.B., Wei, Y.Q., Peng, H.Q., Hu, Z.D., Lu, D., Cui, X.D., Tang, J.** Morphological Effects on the Electrochemical Dissolution Behavior of Forged and Additive Manufactured Ti-6Al-4V Alloys in Runway Deicing Fluid *Surface and Coatings Technology* 414 2021: pp. 127096. https://doi.org/10.1016/j.surfcoat.2021.127096